



## Uncertainty quantification of deep learning model for mineral prospectivity mapping

Ziye Wang, Renguang Zuo

State Key Laboratory of Geological Processes and Mineral Resources, China University of  
5 Geosciences, Wuhan 430074, China

*Correspondence to:* Renguang Zuo (zrguang@cug.edu.cn)

**Abstract.** Deep learning techniques have significantly advanced mineral prospectivity mapping (MPM) by facilitating automated feature extraction and capturing nonlinear relationships among multi-source  
10 geological datasets. However, most deep learning models in MPM neglect the intrinsic uncertainties arising from incomplete geological knowledge, limited sampling, and model variability, leading to overconfident and potentially unreliable predictions. To address this limitation, this study proposes a comprehensive uncertainty quantification framework that jointly evaluates data, model, and prediction uncertainties in deep learning-based MPM. Data uncertainty, originating from sparse of  
15 geochemical/geophysical sampling and subjective interpretations of geological features, is characterized through stochastic simulation of evidential layers. Model uncertainty, arising from variability in network architecture and parameters estimation, is captured through a Bayesian convolutional neural network (CNN) employing Monte Carlo Dropout. The proposed framework is demonstrated through a real-world case study of gold prospectivity mapping in western Henan  
20 Province, China. These uncertainties are quantified using statistical measures including mean, variance, and entropy. The results indicate that areas exhibiting high prospectivity and low uncertainty represent robust and reliable exploration targets, whereas those with high uncertainty highlight regions requiring improved metallogenic interpretation or model refinement. Furthermore, uncertainty contribution analysis reveals that data uncertainty contributes more to total prediction uncertainty than model  
25 uncertainty, suggesting that enhancing the quality and representativeness of evidence layers is more effective for reducing uncertainty than merely optimizing network architecture or parameters. Overall, by modeling and visualizing both data and model uncertainties, the proposed framework transforms deep learning-based MPM from deterministic prediction to probabilistic decision-making, thereby enabling more reliable and trustworthy mineral exploration.



## 30 **1 Introduction**

Mineral prospectivity mapping (MPM) refers to the application of predictive models to analyze and integrate geological datasets for identifying areas that may host undiscovered mineral resources (Bonham-Carter, 1994). Methodologies for MPM have progressed from traditional statistical analysis to machine learning techniques and, more recently, highlight deep learning algorithms as the dominant  
35 paradigm (Carranza, 2008; Zuo, 2020; Zuo et al., 2023; Yang et al., 2024). Compared with traditional approaches, deep learning algorithms are capable of progressively and automatically extracting high-level representations from multi-source geological data, enabling a more comprehensive understanding of complex and nonlinear mineralization processes (Zuo et al., 2019, 2024, 2025).

A wide range of deep learning techniques has been applied in MPM, including autoencoders,  
40 convolutional neural networks (CNNs), generative adversarial networks, graph neural networks, recurrent neural networks, and reinforcement learning (Xiong and Zuo, 2016; Xiong et al., 2018; Li et al., 2022; Yin et al., 2022; Zuo and Xu, 2023; Shi et al., 2023; Yang and Zuo, 2024). Although these methods offer substantial advantages, however, a critical challenge remains: most deep learning models in MPM overlook inherent sources of uncertainty, resulting in overconfident predictions. Typically, the  
45 workflow of deep learning-based MPM involves: (1) developing a conceptual metallogenic model; (2) collecting and preprocessing multi-source geological data; (3) constructing evidential layers with the help of GIS; and (4) integrating these evidential layers to produce a prospectivity map (Zuo, 2020). Due to the multiple interpretations of geological knowledge, limited sampling, and biased predictive models, uncertainties may arise at every stage of this workflow (Zuo et al., 2015, 2021). Moreover,  
50 these uncertainties can propagate and accumulate throughout subsequent stages, ultimately leading to unreliable prospectivity predictions.

Quantifying uncertainty is a critical task in supporting decision-making for MPM. Bárdossy and Fodor (2001, 2004) defined uncertainty as the recognition that measurements and observations may deviate from natural reality, reflecting the imperfect and incomplete nature of human knowledge. Zuo et al.  
55 (2021) systematically categorized the sources of uncertainty in MPM into four types: (1) conceptual model uncertainty, arising from incomplete or simplified understanding of mineralization processes; (2) predictive data uncertainty, caused by sampling errors, measurement biases, and missing data; (3) predictive variable uncertainty, associated with feature selection and the construction of evidential



layers; (4) data integration uncertainty, stemming from parameter optimization, idealized assumptions,  
60 and inadequate data mining within predictive models.

In general, quantifying uncertainty is essential for addressing two key questions: where uncertainty  
arises and how it can be evaluated (Wang et al., 2025). In the context of MPM, uncertainty is  
commonly categorized into two types: aleatoric and epistemic (Hüllermeier and Waegeman, 2021).  
Aleatoric uncertainty, often termed data-related uncertainty, arises from intrinsic noise in data such as  
65 limited sampling, measurement errors, and observation inaccuracies. In contrast, epistemic uncertainty,  
or model-related uncertainty, originates from incomplete knowledge of both the mineralization  
processes and the prediction model. Specifically, mineralization model uncertainty often results from  
cognitive bias and oversimplification of geological processes, whereas prediction model uncertainty  
comes from incomplete training, suboptimal model design, or poor generalization capability (Burkin et  
70 al., 2019; Lindi et al., 2024).

This study focuses on the quantification of data uncertainty and model uncertainty in MPM. Data  
uncertainty considers limited sampling, observational errors, and the selection of negative samples,  
which is primarily expressed during the construction of evidential features, including ore-controlling  
geological structures, geochemical anomalies, and geophysical anomalies. Model uncertainty considers  
75 the variability in deep learning architecture and parameters used to integrate these evidential features.  
Mineralization is controlled by a variety of geological features. For geological evidence features (e.g.,  
faults, intrusions, and formation), discretization is often performed by classifying them into categorical  
units and assigning corresponding weights. Traditional approaches such as the weights-of-evidence  
model (Agterberg et al., 1993) usually assign binary weights (0 or 1) based on the presence or absence  
80 of mineral deposits, thereby introducing uncertainty due to subjective interpretations of mineralization  
processes. Improved approaches like fuzzy logic method (Cheng and Agterberg, 1999; Lisitsin et al.,  
2014) overcome this limitation by assigning continuous weights ranging from 0 to 1, which more  
realistically represent geological facts. For geochemical and geophysical evidence features, discrete  
sampling points are typically transformed into continuous grids using interpolation methods such as  
85 kriging and inverse distance weighting. However, when sampling density is low, these interpolation  
approaches tend to oversmooth the data and can introduce biased estimates in unsampled locations.  
Geostatistical simulation mitigate this limitation by modeling the probability distributions of values in  
unsampled areas, thereby effectively capturing complex multi-point spatial structures in discrete data



and quantifying uncertainty caused by missing data (Wang and Zuo, 2019; Liu et al., 2019).  
90 Additionally, data-driven MPM generally relies on both positive and negative training samples.  
Positive samples are typically derived from known mineral deposit locations, whereas negative samples  
are commonly constructed from randomly selected background points, which can introduce additional  
uncertainty into the modeling process (Carranza et al., 2008). Previous research has shown that the  
approach used to define non-mineralized samples can substantially affect the predictive performance of  
95 MPM (Zuo and Wang, 2020).

For model uncertainty quantification, Bayesian neural networks have emerged as one of the most  
widely used approaches (Gawlikowski et al., 2023). In traditional deep learning models, network  
parameters are treated as deterministic values optimized during training. Although this approach often  
yields high predictive accuracy, it can also lead to overconfident and potentially unreliable predictions,  
100 especially when dealing with noisy or limited training datasets. Bayesian neural networks provide an  
effective solution to this issue by incorporating probabilistic modeling into the neural network  
architecture (Wang and Yeung, 2020; Abdar et al., 2021; Mena et al., 2021). Rather than treating  
network parameters as fixed values, Bayesian neural networks represent them as prior probability  
distributions, thereby capturing uncertainty by estimating the corresponding posterior distributions. To  
105 approximate the intractable posterior distribution of network parameters, various techniques have been  
developed, including Markov Chain Monte Carlo (Gilks et al., 1995), variational inference (Blei et al.,  
2017), and Monte Carlo Dropout (Gal and Ghahramani, 2016). These approaches have been  
successfully applied in Bayesian neural networks (Shridhar et al., 2019; Fakour et al., 2024). Among  
them, Monte Carlo Dropout stands out as a remarkably practical and computationally efficient method  
110 for approximating Bayesian inference (Gal, 2016; Gal and Ghahramani, 2016). Originally introduced  
as a regularization technique to mitigate overfitting, dropout works by randomly disabling subsets of  
neurons during the training phase. At inference time, multiple stochastic forward passes are performed  
with different dropout masks, producing an ensemble of predictions. The variability among these  
predictions reflects the model uncertainty associated with the network architecture and parameter  
115 estimation (Wang et al., 2025).

In summary, this study proposes an uncertainty quantification framework for MPM. The framework  
jointly simulates data uncertainty from evidential layers construction and negative training sample  
selection, as well as model uncertainty caused by variability in network architecture and parameters.



The main contributions are: (1) integrating Monte Carlo Dropout into a CNN to construct a Bayesian  
120 deep learning model for MPM; (2) quantifying both data and deep learning model uncertainties using  
statistical measures such as mean, variance, and entropy; (3) performing contribution analyses to  
evaluate the relative influence of different uncertainty sources on the overall prediction uncertainty. The  
proposed framework is illustrated through a real-world case study of gold prospectivity mapping in  
western Henan Province, China, enabling the delineation of more reliable and trustworthy mineral  
125 prospective areas based on quantified uncertainties.

## 2 Methodology

### 2.1 Data uncertainty modeling

Mineralization is controlled by the combined influence of multiple geological factors, including  
130 geological, geochemical, and geophysical features. For example, faults often serve as pathways for  
fluid migration, intrusions supply heat sources and mineralizing materials, and formations create  
favorable conditions for mineral precipitation. Geochemical and geophysical data also provide essential  
indicators in mineral exploration. In deep learning-based MPM, these ore-controlling geological  
features should be first transformed into evidential layers according to mineralization models, which  
135 are then integrated to predict mineral potential by learning their relationships with known  
mineralization. However, this process inherently introduces uncertainty due to incomplete  
understanding of mineralization processes, insufficient sampling density, and training dataset  
construction. In this study, data uncertainty is represented by stochastic simulation of evidential layers,  
including geological, geochemical, and geophysical features.

140

#### 2.1.1 Geological evidential layers simulation: multifractal singularity

Geological evidential layers are commonly constructed by discretizing geological features with  
weighting function. To simulate the uncertainty associated with this process, multifractal singularity  
theory offers a rigorous mathematical foundation. Within this perspective, mineralization is viewed as a  
145 singular geological phenomenon, marked by the localized concentration of energy or matter within a  
constrained spatiotemporal domain (Cheng, 2007). Under the framework of multifractal singularity



theory, the relationship between mineral deposit density ( $\rho$ ) and the scale ( $\varepsilon$ ), defined as the distance to specific geological features, exhibits fractal behavior in two-dimensional space. This relationship can be expressed by a power-law function (Zuo, 2016; Wang and Zuo, 2022):

150  $\rho = c\varepsilon^{-D}, (1)$

where  $D$  denotes the fractal dimension and  $c$  is a constant. The fractal dimension has proven effective for quantifying the spatial association between mineral deposits and geological features, thereby facilitating the construction of weighting functions for various geological evidential features with the help of GIS (Zuo, 2016). Generally, for a given location  $(i, j)$  near a geological feature, areas closer to the feature tend to contain more significant mineralization information and should therefore be assigned higher weights. Conversely, areas farther away are less relevant, or even irrelevant to mineralization, should be assigned lower weights. Accordingly, the weighting function for an evidential feature can be expressed as a piecewise formula (Wang et al., 2020):

155  $\omega_{ij} = \begin{cases} cd^{-D} & d \leq d_m \\ 0 & d > d_m \end{cases}, (2)$

160 where  $d$  denotes the distance from a given location  $(i, j)$  to the geological feature,  $d_m$  represents the maximum effective controlling distances of that feature. The weight  $\omega$  quantifies the relative contribution of the geological feature to mineralization, with a larger  $\omega$  indicating stronger ore-controlling effect. In practice, the weight  $\omega$  can be estimated by fitting a linear relationship to the log-log plot of  $\rho$  versus  $d$  using the least-squares method (Wang et al., 2015):

165  $\log(\rho) = -\omega \log(d) + c. (3)$

The distance  $d_m$ , also known as the spatial extent of a feature's influence, is typically estimated empirically based on metallogenic models, which vary according to expert interpretation. This subjectivity inevitably introduces data uncertainty into MPM (Wang and Zuo, 2022). Consequently, the uncertainty of geological evidential features can be modeled by randomly sampling the parameter  $d_m$

170 within a predefined interval (Figure 1).

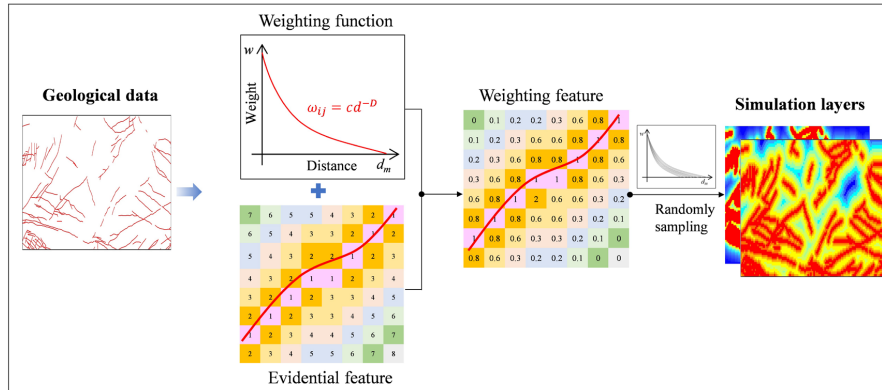


**Figure 1: Simplified workflow of data uncertainty modeling: geological evidential layers simulation.**

175 **2.1.2 Geochemical and geophysical evidential layers simulation: direct sampling**

Grid construction from discrete samples is a fundamental step in generating geochemical and geophysical evidence features. Unlike conventional interpolation methods, the direct sampling (DS) multiple-point statistical technique has gained prominence attention for its ability to construct continuous evidential maps while incorporating uncertainties at unsampled locations (Mariethoz et al., 2010; Meerschman et al., 2013; Wang et al., 2023). Theoretically, DS is designed to directly match data events from the simulation grid with spatial patterns in a training image (TI), thereby producing realizations that preserve realistic spatial structures (Hosseini et al., 2021).

Let  $G$  denote the simulation grid,  $z(x_i)$  represent the observed value at location  $x_i$ , and  $D = \{(x_i, z(x_i))\}_{i=1}^n$  belong to the set of  $n$  conditioning data. The goal of DS is to estimate  $z(x)$  for all unsampled locations  $x$ . At each unsampled node, a data event is defined as the set of conditioning nodes within a specified neighborhood around  $x$ . In the training image TI, DS commonly employs the normalized mean squared error to quantify the similarity between the simulation data event and the TI pattern. Given a similarity threshold  $t$ , DS sequentially scans the TI until the distance between an observed data event and a TI pattern falls below the threshold  $t$ . Then, the value at the central node of the matched TI pattern is assigned to the simulation node. If no sufficiently similar pattern is found after scanning a maximum fraction  $f$  of the TI, the value from the best-matched pattern encountered is used instead. DS addresses this type of uncertainty by generating multiple geochemical and



geophysical realizations, each honoring the conditioning data but differing in local spatial details due to stochastic sampling. This process transforms discrete samples into gridded maps that, on the one hand, alleviate smoothing effects at unsampled locations and, on the other hand, incorporate uncertainty arising from missing data and sparse sampling (Yang et al., 2023; Wang et al., 2023) (Figure 2).

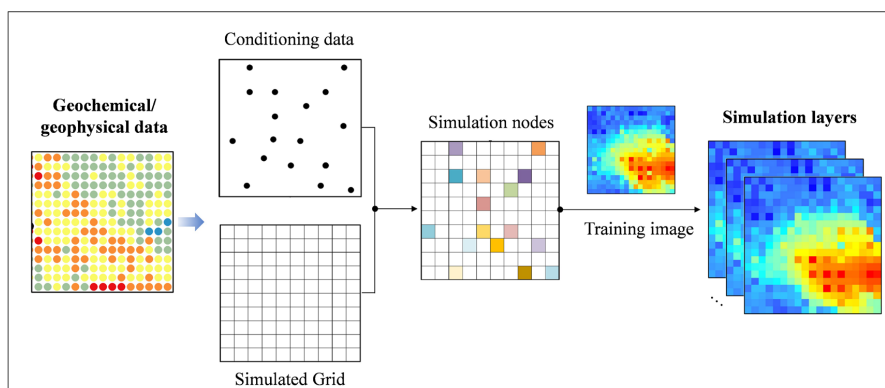


**Figure 2: Simplified workflow of data uncertainty modeling: geochemical and geophysical evidential layers simulation.**

200

### 2.2 Negative training samples: random generation

CNNs rely on both positive and negative samples to learn discriminative features that distinguish mineralization from non-mineralized backgrounds. In practice, known mineral deposit locations are used as positive samples, while negative samples are typically selected randomly from non-mineralized areas (Carranza et al., 2008). However, the definition of non-mineralized regions is inherently uncertain, as geological processes are continuous and ore-forming environments may extend beyond the boundaries of known deposits. In this study, the uncertainty associated with negative samples selection is modeled by randomly sampling points from regions located far from known deposits, ensuring minimize potential mineralization influence. The effects of negative sample selection on model performance can then be quantified, thereby providing a measure of data uncertainty arising from sample preparation.

210

### 2.3 Model uncertainty modeling

#### 2.3.1 Bayesian CNN



215 CNNs can automatically extract low-level features, which are progressively combined into higher-level  
representations describing complex spatial patterns (Gu et al., 2018). A standard CNN architecture  
comprises a sequence of convolutional, pooling, and fully connected layers (Figure 3a). The  
convolutional layers are responsible for capturing local spatial patterns using learnable filters; the  
pooling layers downsample feature maps, thereby lowering computational cost and helping to prevent  
220 overfitting. The fully connected layers then aggregate the extracted features into a global representation  
for final prediction. This hierarchical progression from low-level to high-level feature representations  
makes CNNs particularly effective for integrating diverse spatial evidential layers in MPM.

Bayesian CNNs extend traditional CNNs by incorporating Bayesian inference to model uncertainty in  
both network parameters and predictions (Gal and Ghahramani, 2015; Shridhar, 2019). Bayesian CNNs  
225 share similar architectures with standard CNN while treat network weights as random variables defined  
by probability distributions. This probabilistic framework enables the network to learn complex,  
nonlinear feature representations while simultaneously quantifying model uncertainty. During training,  
Bayesian inference approximates the posterior distribution of network parameters. At inference time,  
multiple stochastic forward passes are conducted to produce a distribution of predictions, thereby  
230 enabling the estimation of model uncertainty.

### 2.3.2 Monte Carlo dropout

Bayesian inference provides a theoretical framework for modeling parameter uncertainty and  
propagating it into model uncertainty. However, exact Bayesian inference in neural networks is  
235 intractable due to high-dimensional parameter spaces. Monte Carlo Dropout is a practical and  
computationally efficient means to approximate Bayesian inference, without explicitly learning  
probability distributions over network weights (Gal and Ghahramani, 2016; Seoh, 2020) (Figure 3b).  
Originally introduced as a regularization technique, dropout works by randomly deactivating neurons  
during training with a specified probability. In the Bayesian interpretation, this process can be viewed  
240 as sampling from a distribution over network parameters. During inference, dropout is kept active and  
multiple stochastic forward passes are performed for the same input, each corresponding to a different  
thinned subnetwork. The resulting ensemble of predictions forms an approximate posterior predictive  
distribution, enabling the estimation of model uncertainty. Importantly, Monte Carlo Dropout provides



a lightweight, scalable, and easily implementable approach to Bayesian deep learning by simply adding  
 245 dropout layers before each pooling layer in a standard CNN architecture.

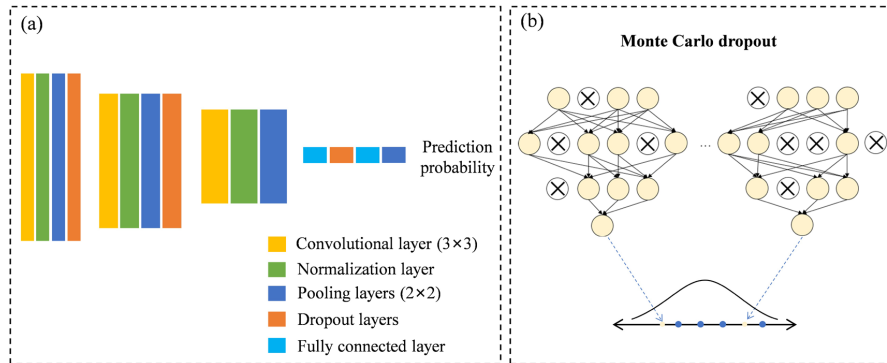


**Figure 3: Simplified workflow of model uncertainty modeling: (a) Bayesian CNN, (b) Monte Carlo dropout.**

250 **2.4 Uncertainty quantification metrics**

For uncertainty quantification, variance and entropy are two of the most widely used statistical measures. Given  $T$  stochastic predictions  $\{p_t\}_{t=1}^T$ , where  $p_t$  is the probability predicted by the Bayesian CNN, the variance can be expressed as:

$$Var(p) = \frac{1}{T} \sum_{t=1}^T (p_t - \bar{p})^2, \quad (4)$$

255 where  $\bar{p}$  denotes the mean prediction across all  $T$  forward passes at each location  $(i, j)$ . Variance reflects the dispersion of predictions around the mean, indicating the degree of disagreement among stochastic realizations.

Entropy, introduced by Shannon (1948) in information theory, measures the expected amount of information contained in a probability distribution. It has been extensively applied in geoscientific modeling to characterize uncertainty in spatial predictions (Wellmann and Regenauer-Lieb, 2012).

260 Mathematically, entropy is defined as:

$$H(p) = - \sum_{t=1}^T p_t \log p_t. \quad (5)$$

In this study, entropy quantifies the expected uncertainty of the predicted probability distribution for mineral occurrence. Thus, a higher entropy value indicates a more diffuse probability distribution, reflecting greater uncertainty and a lower level of confidence in the predicted mineralization potential.  
 265



### 3 Study area and dataset

#### 3.1 Geological setting

The case study area is situated in western Henan Province, China (Figure 4). This region is recognized as one of the country's most important gold-producing areas, hosting more than 81 large to super-large gold deposits (Deng and Wang, 2016; Fan et al., 2016; Zhang et al., 2020). Such findings highlight substantial potential for further gold exploration (Mao et al., 2002, 2005; Tang et al., 2013). The gold deposits are predominantly magmatic-hydrothermal in origin, formed mainly during the Early Cretaceous under an extensional tectonic regime of the Yanshanian period. According to the established metallogenic models, mineralization and its spatial distribution are primarily controlled by regional faults, Yanshanian igneous intrusions, and the strata of the Xiong'er and Taihua rock groups. Specifically, ore-forming materials are sourced from the deep mantle, while intrusions of intermediate to acidic magmatic rocks supplied the thermal energy for fluid migration. Faults served as major conduits for fluid transport, ultimately leading to gold mineralization within the Taihua and Xiong'er Group formations (Mao et al., 2002; Wu et al., 2012; Pang et al., 2020). Furthermore, aeromagnetic data offer indirect geophysical evidence, whereas geochemical data provide direct evidence of elemental anomalies linked to gold mineralization.

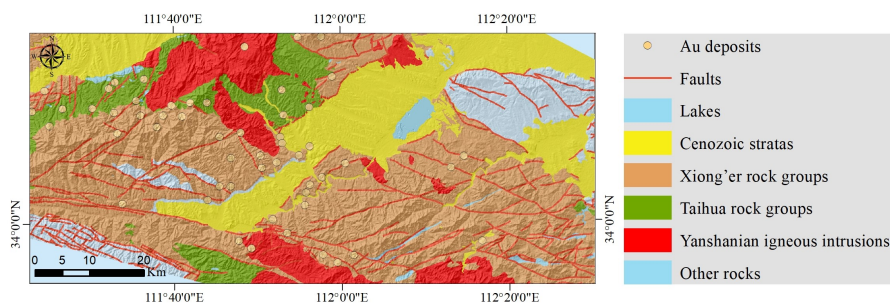


Figure 4: Simplified geological map of the study area.

285

#### 3.2 Dataset

The geochemical exploration dataset was sourced from the Chinese National Geochemical Mapping

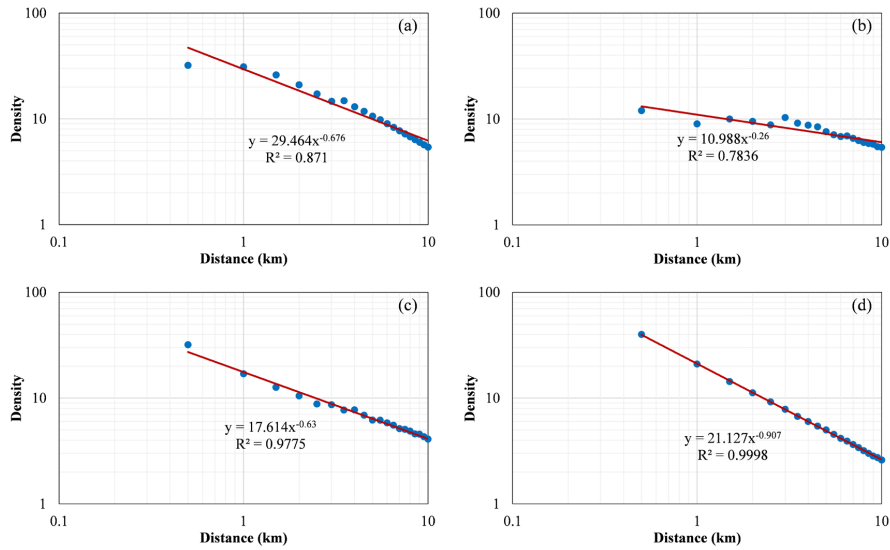


Project (Xie et al., 1997), comprising of 1,131 stream sediment samples collected at a 1:200,000 scale. Each sample contains concentrations of 39 major and trace elements, determined using analytical techniques such as inductively coupled plasma atomic fluorescence spectrometry, X-ray fluorescence, and inductively coupled plasma atomic emission spectrometry. Geochemical data are typical compositional data, which can induce false spatial and statistical correlations among elements. Accordingly, geochemical exploration data were preprocessed using centered-log ratio transformations to eliminate the influence of closure effects (Aitchison, 1986). The geophysical data comprises aeromagnetic data at the same scale. To reduce distortions associated with skewed magnetization, vertical first-order derivatives were applied to enhance shallow magnetic anomaly signatures. Consequently, 44 metallogenic-related evidential features, including faults, Yanshanian igneous intrusions, Xiong'er and Taihua rock groups strata, geophysical aeromagnetic data, and 39-element geochemical data, are extracted to construct the evidential layers for MPM (Fan et al., 2023; Yang and Zuo, 2024; Yang et al., 2024).

#### 4 Evidential layers simulation

##### 4.1 Geological evidential layers simulation

The generation of geological evidence layers relies on buffer analysis combined with weighting functions. This procedure involves counting the number of mineral deposits that fall within different buffer zones surrounding geological features, thereby quantitatively characterizing their spatial correlation with mineralization. The resulting spatial correlation patterns are subsequently used to derive weighting functions for corresponding evidence layers. Specifically, fractal dimensions  $D$  are calculated from log-log plots of paired datasets  $[\rho, d]$ , yielding values of 0.676, 0.260, 0.907, and 0.630 for faults (Figure 5a), Yanshanian igneous intrusions (Figure 5b), and the Xiong'er (Figure 5c) and Taihua (Figure 5d) rock groups strata, respectively. Fractal analysis suggests that the Xiong'er group strata and faults exert a stronger spatial influence on gold mineralization compared with other geological features. This finding is consistent with established metallogenic models and existing geological knowledge, thereby supporting the reliability of the geological evidence layer construction.



315

**Figure 5: Log–log plots of deposits density vs. buffer width: (a) faults, (b) Yanshanian igneous intrusions, (c) Taihua rock groups strata, (d) Xiong'er rock groups strata.**

In the weighting function, the uncertain parameter  $d_m$ , representing the maximum controlling distance of a geological feature, is empirically assigned as a random value within the estimated interval [5, 10]. Accordingly, the weighting function for these geological features is expressed as:

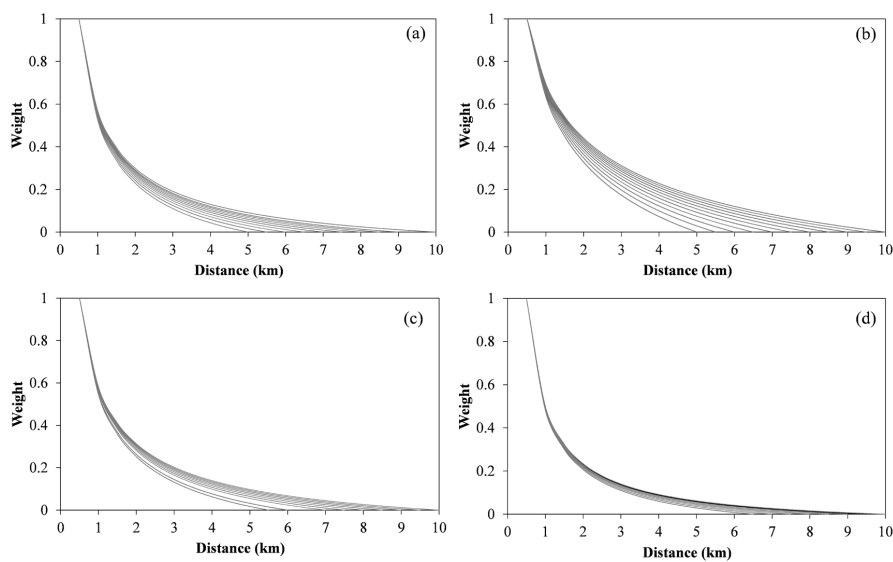
$$\omega = \frac{1}{1-d_m^{-D}} (x^{-D} - d_m), d_m \in [5, 10]. \quad (6)$$

This formulation accounts for both the relative influence of geological features on mineralization and the uncertainty inherent in the modeling process. The resulting weight values range continuously from 1 and 0. A weight of 1 indicates a strong statistical correlation between the geological feature and known mineral deposits, whereas decreasing values represent weaker spatial association. When the location  $x$  exceeds the maximum controlling distances  $d_m$ , the weight reduces to 0, implying that the geological feature in those regions exerts no measurable impact on mineralization. To incorporate uncertainty into the weighting process, Monte Carlo sampling is performed by randomly selecting  $d_m$  values from the defined intervals, generating 100 weighting functions (Figure 6) and corresponding weighted evidential layers for each geological feature (Figure 7). These multiple realizations not only capture the variability arising from parameter uncertainty but also provide a probabilistic representation of the spatial relationships between geological features and mineralization, thereby offering a more

330

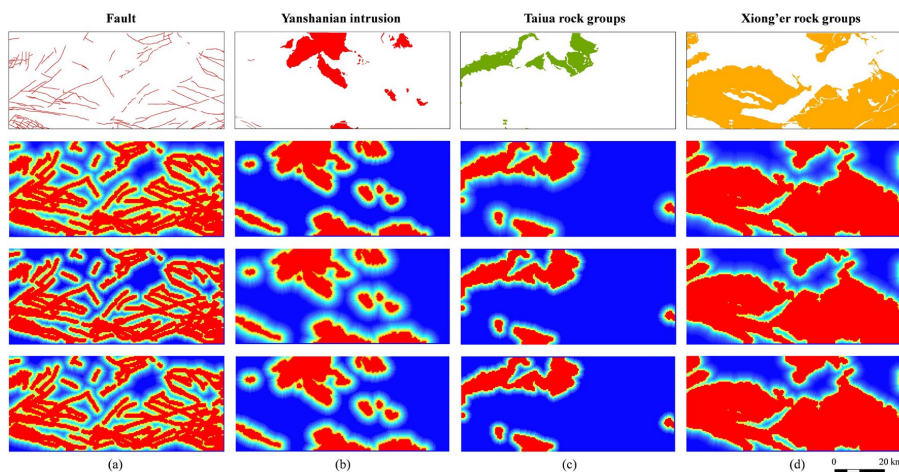


robust characterization of data uncertainty.



335

Figure 6: Weighting functions curves: (a) faults, (b) Yanshanian igneous intrusions, (c) Taihua rock groups strata, (d) Xiong'er rock groups strata.



340

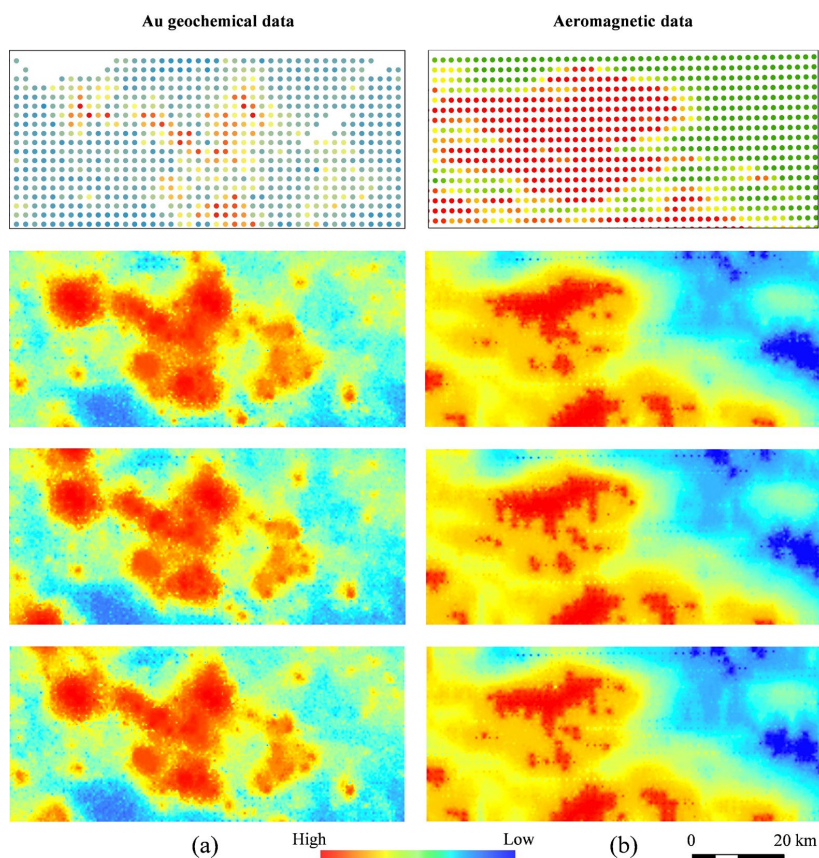
Figure 7: Three randomly selected weighted evidence layers: (a) faults, (b) Yanshanian igneous intrusions, (c) Taihua rock groups strata, (d) Xiong'er rock groups strata.

#### 4.2 Geochemical and geophysical evidential layers simulation



To model the spatial distribution patterns of geochemical elements, the DS algorithm is employed to  
345 interpolate element concentrations at unsampled locations, thereby transforming discrete geochemical  
measurements into spatially continuous evidential layers. In this study, geochemical values at sampling  
points serve as both conditioning data and the TI for the simulation process. Two parameters, the  
similarity threshold  $t$  and the maximum fraction  $f$  of the TI to be scanned, are empirically set to 0.1  
and 0.7, respectively. In this regard, a total of 100 realizations of geochemical maps are generated, each  
350 representing an independently simulated spatial distribution pattern of element concentrations. These  
multiple simulations provide alternative possible values at unsampled locations, thus accounting for the  
uncertainty arising from sparse and uneven sampling. The spatial distribution of Au geochemical  
samples and three randomly selected simulated evidential layers are shown in Figure 8a. Geophysical  
evidence layers are produced following the same simulation procedure. Figure 8b presents three  
355 representative simulated aeromagnetic evidence layers.

Furthermore, to evaluate the reliability of the simulations, cumulative frequency distribution curves are  
employed to compare the similarity between observed and simulated patterns. Using Au as an example,  
the results (Figure 9) clearly demonstrate that the DS successfully reproduces the spatial distribution  
pattern of geochemical features in the study area, enabling the generation of realistic geochemical  
360 evidence layers while simultaneously accounting for uncertainty associated with unsampled regions. In  
total, 44 evidence layers are constructed as model inputs, including geological features (faults,  
intrusions, strata), aeromagnetic data, and geochemical data comprising 39 elemental concentration  
maps. Each evidential layer is simulated 100 times, providing sufficient realizations to quantify both  
data uncertainty and model uncertainty in MPM.



365

Figure 8: Three randomly selected simulated evidence layers: (a) Au geochemical layer, (b) geophysical aeromagnetic layer.

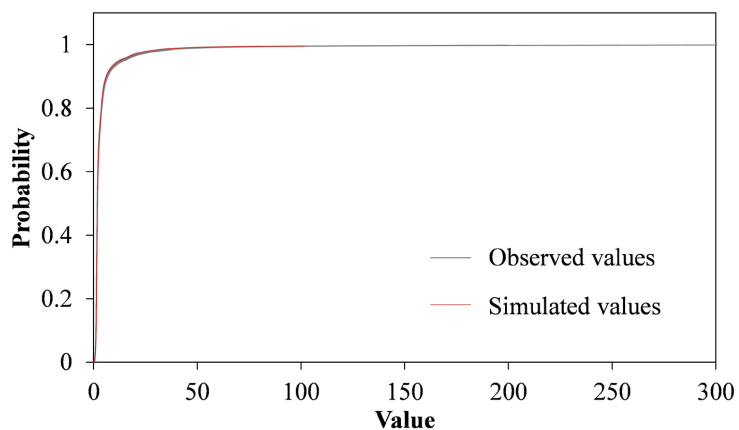


Figure 9: Cumulative frequency distribution curves derived from 100 simulated Au geochemical layers.

370



## 5 Experimental setting

### 5.1 Network architecture and parameters

The Bayesian CNN architecture (Table 1) comprises three  $3 \times 3$  convolutional layers, three normalization layers, two  $2 \times 2$  max-pooling layers, and two fully connected layers. Each convolutional layer is followed by a dropout layer to facilitate uncertainty estimation. The final output layer employs a sigmoid activation function to produce probability predictions for MPM. Key hyperparameters, including the learning rate, batch size, number of epochs, activation function, and optimizer, are list in Table 2. Model performance is evaluated using binary cross-entropy loss and classification accuracy. It should be noted that the sensitivity analysis of these parameters is beyond the scope of the present study.

**Table 1: Network architecture of the Bayesian CNN.**

Layer name	Number	Filter size	Feature dimensions
Input	/	/	$9 \times 9 \times 44$
Convolution layer	16	$3 \times 3$	$9 \times 9 \times 44$
Batch normalization			$9 \times 9 \times 44$
Dropout layer			
Max pooling layer		$2 \times 2$	$4 \times 4 \times 22$
Convolution layer	32	$3 \times 3$	$4 \times 4 \times 22$
Batch normalization			$4 \times 4 \times 22$
Dropout layer			
Max pooling layer		$2 \times 2$	$2 \times 2 \times 11$
Convolution layer	64	$3 \times 3$	$2 \times 2 \times 11$
Batch normalization			$2 \times 2 \times 11$
Dropout layer			
Fully connected layer			64
Dropout layer			
Fully connected layer			1
SoftMax			1
Output			1



**Table 2: Hyperparameter settings of the Bayesian CNN.**

Layer name	Number	Filter size	Feature dimensions
Input	/	/	$9 \times 9 \times 44$
Convolution layer	16	$3 \times 3$	$9 \times 9 \times 44$
Batch normalization			$9 \times 9 \times 44$
Dropout layer			
Max pooling layer		$2 \times 2$	$4 \times 4 \times 22$
Convolution layer	32	$3 \times 3$	$4 \times 4 \times 22$
Batch normalization			$4 \times 4 \times 22$
Dropout layer			
Max pooling layer		$2 \times 2$	$2 \times 2 \times 11$
Convolution layer	64	$3 \times 3$	$2 \times 2 \times 11$
Batch normalization			$2 \times 2 \times 11$
Dropout layer			
Fully connected layer			64
Dropout layer			
Fully connected layer			1
SoftMax			1
Output			1

390 **5.2 Sample preparation**

CNNs can capture the spatial patterns embedded in geoscientific data. Accordingly, a  $9 \times 9$  sliding window is used to draw training samples from the evidential layers. This approach ensures that each training sample encompasses not only the central pixel but also the contextual information from its surrounding  $9 \times 9$  neighborhood. Within this window, each pixel is characterized by 44 evidential features derived from geological, geochemical, and geophysical datasets, forming a comprehensive feature space that enables the CNN to learn spatial-attribute relationships associated with mineralization. A total of 483 positive samples with dimensions of  $9 \times 9 \times 44$  are extracted from 51 known gold deposits and their surrounding neighborhoods within a  $3 \times 3$  km radius. This data augmentation strategy has been demonstrated effectively to improve the generalization ability of deep learning algorithms in MPM (Zuo, 2025). To ensure dataset balance, an equal number of negative samples are also randomly generated from areas distant from known mineralization during each training stage. Of the total samples, 80% are used for model training, while the remaining 20% are reserved for validation.

405 **6 Result**

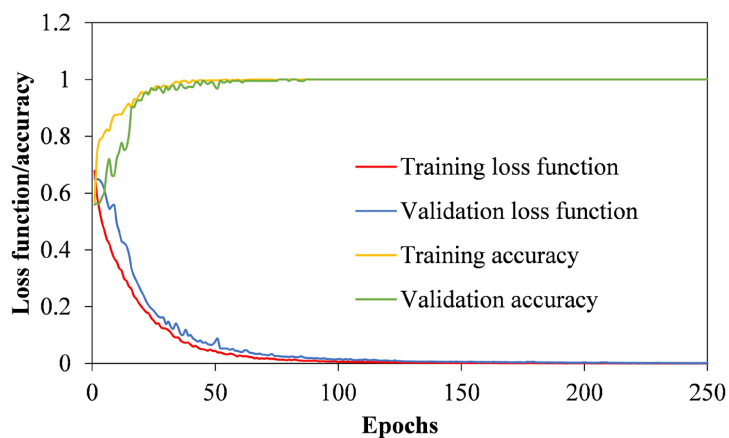


This study proposes a framework to quantify and visualize uncertainty in MPM by jointly modeling data uncertainty via stochastic simulation of evidence layers and model uncertainty via Monte Carlo dropout. To evaluate the influence of different uncertainty sources on MPM, four comparative case studies are designed: (1) deterministic CNN, (2) data uncertainty quantification, (3) model uncertainty  
410 quantification, and (4) total prediction uncertainty quantification that integrates both data and model uncertainties. Each case is structured to isolate or combine specific sources of uncertainty while keeping all other factors constant, allowing a systematic assessment of how data uncertainty, model uncertainty, and their combination affect prediction stability and reliability. All cases adopt identical network architectures, parameters, and evaluation metrics to ensure fair comparison.

415

### 6.1 Deterministic CNN

A deterministic CNN is first trained using the original evidence layers to validate the effectiveness of the proposed network architecture and parameters settings. The training convergence curves of loss and accuracy over epochs (Figure 10) indicate that the deterministic model achieved stable and satisfactory  
420 training performance. The resulting prospectivity map of gold deposits (Figure 11) reveals that high-potential areas closely align with the spatial distribution of known deposits, which in agreement with established geological understanding. The outcomes provide additional evidence supporting the reliability and efficacy of the proposed CNN architecture for MPM.



425 **Figure 10: Convergence curves of training loss and accuracy across epochs for the deterministic CNN.**

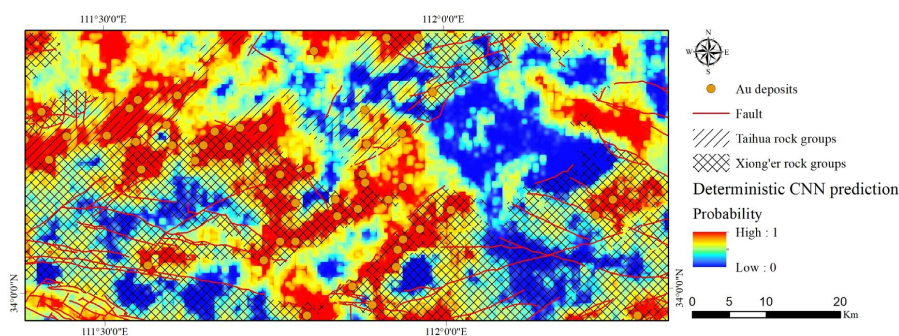


**Figure 11: Mineral prospectivity map obtained by the deterministic CNN.**

430

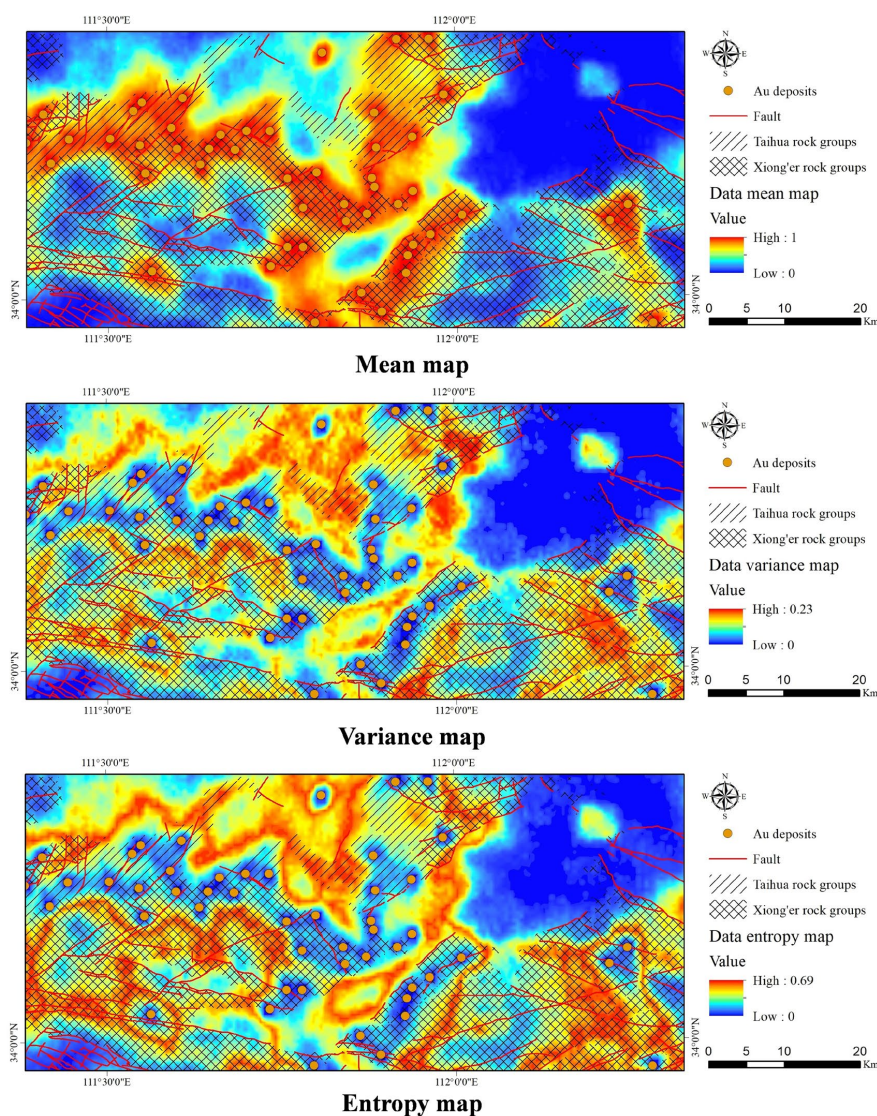
## 6.2 Data uncertainty quantification

Data uncertainty is quantified by generating multiple simulated evidence layers with randomly generated negative samples, thereby capturing variability arising from incomplete geological knowledge, limited sampling density, and randomness of training labels. A deterministic CNN model is trained on simulated evidence layers to produce 100 prospectivity predictions. Figure 12 presents the mean, variance, and entropy maps across these predictions. The mean map (Figure 12a) represents the most probable spatial distribution of mineralization potential by averaging the ensemble predictions. High mean values indicate areas of consistently high prospectivity, which are primarily distributed along major faults and within the Xiong'er rock groups strata. These regions closely coincide with known gold deposits, confirming that the CNN model effectively captures the key mineralization patterns. Most deposits in the study area are quartz-vein and altered-rock types, mainly controlled by faults which act as pathways for mineralizing fluids, while the surrounding strata provide favorable host environments, jointly contributing to the high prospectivity in these regions.

The variance and entropy maps reveal different aspects of data uncertainty induced by the stochastic simulation of evidence layers. The variance map (Figure 12b) quantifies the degree of variability among the 100 prospectivity predictions under varying evidence inputs. Regions with low variance indicate stable predictions and high confidence. Conversely, areas with high variance demonstrate strong sensitivity to data perturbations, suggesting that small variations in evidence layers can substantially affect the predicted probabilities. Although both metrics display broadly similar spatial



450 patterns, the entropy map (Figure 12c) offers additional insight beyond variance by characterizing the uncertainty in the probability distribution of predictions. In other words, entropy captures the degree of ambiguity in predictions, even when the magnitude of variation is moderate. Overall, areas exhibiting high mean and low entropy values represent the most reliable exploration targets, while those characterized by high prospectivity but high uncertainty deserve further geological investigation.



455

**Figure 12: Data uncertainty quantification: (a) mean, (b) variance, and (c) entropy maps.**



### 6.3 Model uncertainty quantification

Model uncertainty is quantified using the Bayesian CNN trained on the original evidence layers, reflecting the inherent randomness in network structure and parameters estimation. The resulting mean, variance, and entropy maps (Figure 13) provide a comprehensive view of both prediction outcomes and the associated uncertainty in deep learning-based MPM. High-probability regions in the mean map (Figure 13a) appear primarily distributed within the Xiong'er rock groups, implying geologically favorable conditions for gold mineralization. In contrast, Yanshanian intrusions show relatively low probabilities, suggesting less favorable metallogenic conditions. The strong spatial correspondence between high-probability regions and known Au occurrences confirms that the Bayesian CNN model effectively captures the principal ore-controlling geological features of gold mineralization. The variance and entropy maps (Figure 13b and c) exhibit similar spatial patterns. Areas with low variance and low entropy generally coincide with high mean probabilities and known deposits, reflecting strong model confidence and stable predictive behavior. Conversely, regions with high variance and entropy indicate greater model uncertainty, implying limited model knowledge or insufficient feature representation for reliably inferring mineralization potential in those regions.

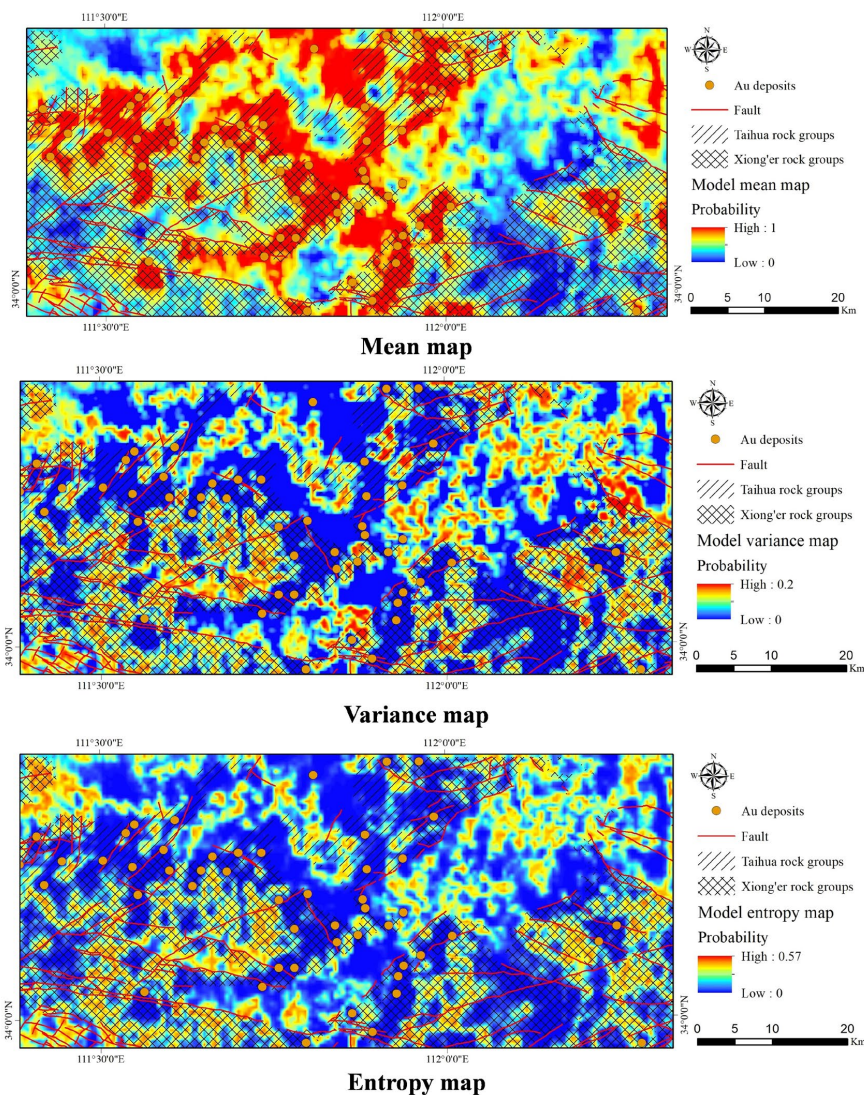


**Figure 13: Model uncertainty quantification: (a) mean, (b) variance, and (c) entropy maps.**

475

Notable differences are observed between the data and model uncertainty maps. Data uncertainty primarily arises from the heterogeneity and stochasticity of evidential layers, whereas model uncertainty reflects the intrinsic limitations of the network in learning stable and generalizable relationships from the available data. Overall, data uncertainty appears broader and more pronounced than model uncertainty, implying that variability in the evidence layers exerts a greater influence than the network structure or parameter settings. This finding further suggests that, in geologically complex

480



regions, the CNN model faces challenges in accurately interpreting gold prospectivity when the input data themselves are highly uncertain.

485 **6.4 Prediction uncertainty quantification**

The total prediction uncertainty represents the combined effects of both data and model uncertainties, derived through stochastic simulation of evidence layers with a Monte Carlo dropout-based Bayesian CNN. In this way, 10,000 predictions are generated, enabling a comprehensive characterization of the overall uncertainty. The mean, variance, and entropy maps are shown in Figure 14. Compared with the  
490 individual uncertainty quantification, the jointly consideration of data and model uncertainties yields smoother and more spatially coherent patterns that align better with the distribution of known Au deposits. The mean prospectivity map (Figure 14a) preserves the main high-prospectivity areas identified in the data and model uncertainties, highlighting the stabilizing effect achieved by combining model stochasticity with variations in evidential inputs. The variance map (Figure 14b) indicates that  
495 the total prediction uncertainty effectively captures variability arising from both geological features and the CNN model, thereby enhancing prediction robustness. The spatial distribution of prediction entropy (Figure 14c) provides direct implications for exploration strategy and model refinement. High entropy regions suggest either input data or model limitations, whereas low entropy areas represent priority targets because the model provides a low-risk prediction indication. Importantly, repeated predictions  
500 allow the model to account for variations in both evidence layers and network architecture, resulting in highly consistent variance and entropy patterns across the study area.

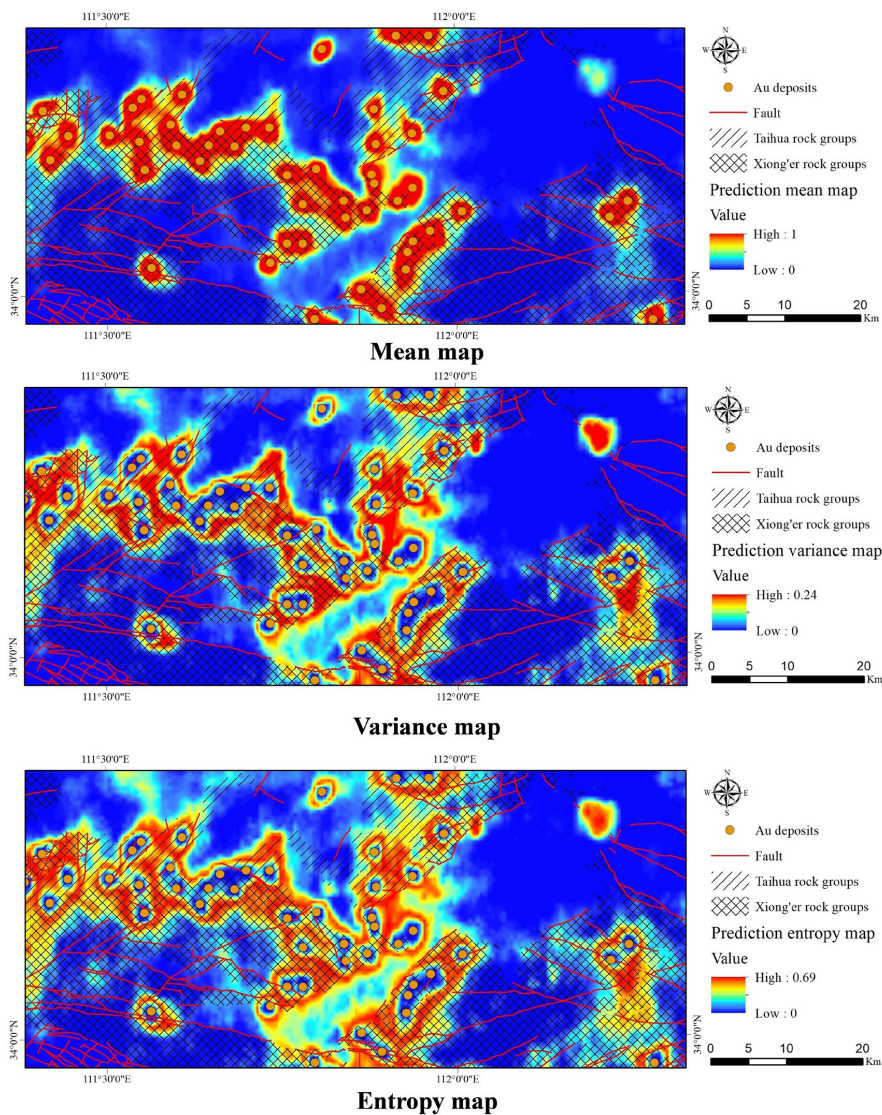


Figure 14: Prediction uncertainty quantification: (a) mean, (b) variance, and (c) entropy maps.

## 505 7 Discussion

### 7.1 Uncertainty decomposition

To quantify the relative contribution of data and model uncertainties to the total prediction uncertainty in MPM, a dominant uncertainty map is presented using variance decomposition. This statistical



approach enables the partitioning of total predictive variance into components attributable to data  
510 variability and model stochasticity, thereby providing a clearer understanding of uncertainty sources  
and supporting more informed exploration decisions. The data uncertainty ( $Var_{data}$ ) exhibits  
geologically meaningful patterns, reflecting the influence of heterogeneous simulated evidence layers.  
In contrast, the model uncertainty ( $Var_{model}$ ) primarily captures limitations of the network architecture  
and parameters, highlighting areas where the CNN struggles to generalize. Then, the relative  
515 contribution of each component can be calculated as their ratio to the total prediction uncertainty  
( $Var_{total}$ ) (Figure 15). Obviously, high data uncertainty (Figure 15a) contribution exhibits broader  
spatial influence, whereas high model uncertainty (Figure 15b) contribution is more localized with  
lower magnitude. This finding suggests that variability within the evidence layers is the primary source  
of total uncertainty. Moreover, the clustering of data uncertainty around known deposits further reflects  
520 its dominant contribution to total uncertainty. Consequently, enhancing the quality and  
representativeness of input evidence layers is likely to be more effective in reducing total MPM  
uncertainty than solely optimizing the CNN architecture or parameters.

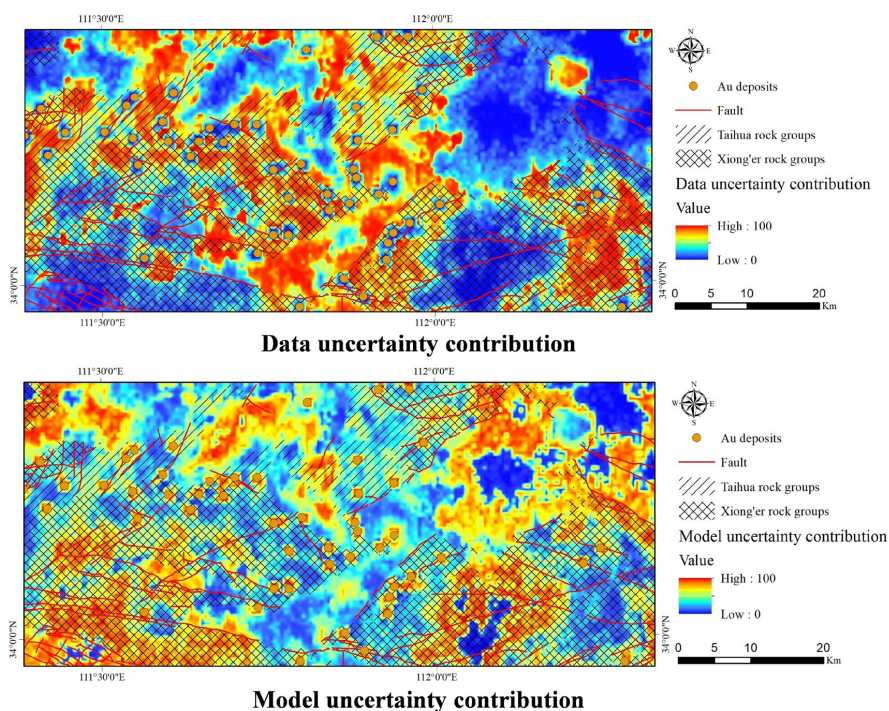
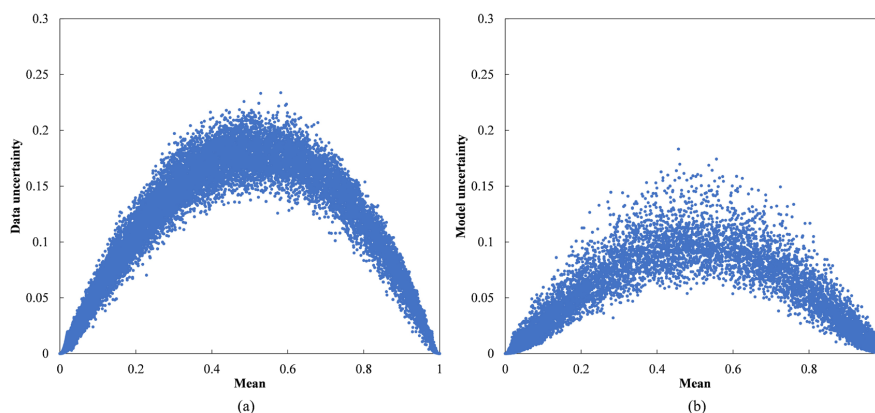


Figure 15: Uncertainty contribution maps: (a) data uncertainty, (b) model uncertainty.

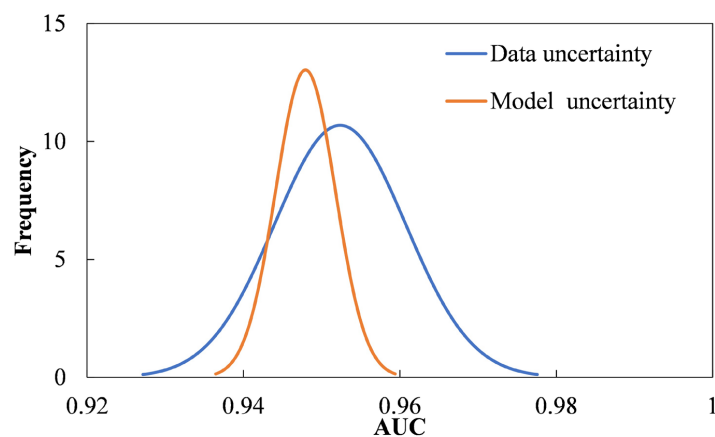


525

The mean-uncertainty scatter plots (Figure 16) exhibit an inverted U-shaped distribution, providing a direct visualization of how data uncertainty and model uncertainty vary with the mean prediction values. Data uncertainty shows a generally higher magnitude than model uncertainty, indicating that variability in the geological evidence layers contributes more substantially to the prediction uncertainty than instability in the model parameters. The area under the receiver operating characteristic curve (AUC) is another robust metric widely adopted to quantitatively measure model performance, particularly in the presence of class imbalance (Chen and Wu, 2016). Figure 17 presents the frequency distribution of AUC values derived from 100 realizations for data uncertainty and model uncertainty. Both distributions are centered around  $AUC \approx 0.95$ , indicating that the CNN model maintains consistently high predictive accuracy across multiple simulations. However, the wider spread of the data uncertainty curve reflects greater variability in predictive performance due to fluctuations in the evidence layers. In contrast, the narrower spread of the model uncertainty curve demonstrates that the network structure and parameters remain relatively stable during stochastic forward passes. Such results further emphasize the importance of optimizing mineralization models and weighting strategy by identifying the most influential geological features, as they exert more influence on prediction uncertainty.



**Figure 16: The mean-uncertainty scatter plots: (a) data uncertainty, (b) model uncertainty.**



545 **Figure 17: Frequency distribution of AUC values: (a) data uncertainty, (b) model uncertainty.**

## 7.2 Geological significance

Uncertainty quantification provides essential insights into the reliability of MPM. On the one hand, it delineates regions characterized by low uncertainty and high prospectivity probability, thereby guiding exploration efforts toward areas with the greatest potential of new mineral discoveries. On the other hand, it reveals the key geological, geochemical, and geophysical factors that most strongly control mineralization, offering a deep understanding of the underlying ore-forming processes. By decomposing total uncertainty into data uncertainty and model uncertainty, the proposed framework establishes a quantitative basis for evaluating the credibility of prediction outcomes. Such differentiation enables the identification of whether uncertainty stems from inappropriate evidence layers or model limitations. Specifically, regions with high prospectivity and low total uncertainty represent high-confidence exploration targets, whereas high uncertainty areas correspond to high-risk but potential opportunities. Consequently, uncertainty quantification not only enhances the interpretability of MPM but also supports informed decision-making in mineral exploration.

560

## 7.3 Future prospects

Future advances in uncertainty quantification for MPM are expected to focus on improvements in data quality, modeling strategies, interpretability, and decision optimization to reduce prediction uncertainty



ultimately. From a data perspective, enhancing the geological representativeness of evidence layers is  
565 critical for reducing data uncertainty and more accurately capturing the spatial variability of  
mineralization controls. Regarding the uncertainty modeling, progress should extend beyond  
conventional Monte Carlo dropout toward Bayesian inference and ensemble learning capable of jointly  
characterizing both data and model uncertainties. In terms of the uncertainty interpretability and  
visualization, embedding geological knowledge directly into deep learning architectures and loss  
570 functions offers a promising way to constrain model training, reduce high-uncertainty output, and  
enhance the transparency of predictions. In addition, feature attribution is also valuable for identifying  
which evidential layers drive most to high prospectivity or high uncertainty, thereby strengthening  
geological interpretability. Finally, integrating uncertainty quantification with risk-return analysis will  
support the selection of exploration targets that balance mineralization potential against geological risk,  
575 translating probabilistic predictions into more actionable decision support.

## 8 Conclusions

This study proposes an integrated framework for uncertainty quantification in deep learning-based  
MPM. The framework quantifies data uncertainty, model uncertainty, total prediction uncertainty, and  
580 is illustrated through a real-world case study of gold prospectivity mapping in western Henan Province,  
China. Uncertainty quantification transforms MPM from a purely predictive approach into a decision-  
support framework, enabling more valuable and risk-aware mineral exploration.

- (1) Data uncertainty in MPM arises from limited sampling density of geochemical and geophysical  
585 data, as well as subjective interpretation of in geological modeling, which is modeled through  
stochastic simulation of evidence layers constrained by geological understanding. Model  
uncertainty reflects variability in network architecture and parameter estimation, which is modeled  
using a Bayesian CNN with Monte Carlo dropout.
- (2) Contribution analysis reveals that data uncertainty is the dominant source of total prediction  
uncertainty in MPM, exhibiting more geologically meaningful patterns than model uncertainty.  
590 This finding indicates that improving the quality and representativeness of evidence layers is more  
effective for reducing overall uncertainty than optimizing the CNN architecture and parameters.
- (3) Uncertainty quantification enhances the reliability of MPM by distinguishing between data- and



model-driven uncertainties. Areas characterized by high prospectivity and low uncertainty  
represent robust exploration targets, while those with high uncertainty highlight regions requiring  
595 improved geological knowledge or further model refinement.

#### Code and Data Availability

The codes and data are provided on Zenodo at <https://doi.org/10.5281/zenodo.18903959> (Wang, 2026).

#### 600 Author contributions

**ZW:** Conceptualization, Methodology, Software, Writing-original draft, Writing-review & editing. **RZ:**  
Writing-review & editing, Supervision.

#### Declaration of Competing Interest

605 The authors declare that they have no conflict of interest.

#### Acknowledgements

This research was jointly supported by the National Science and Technology Major Project for Deep  
Earth Probe and Mineral Resources Exploration (2025ZD1009109), Key Research and Development  
610 Program of Xinjiang Uygur Autonomous Region, China (2024B03010-3), and National Natural  
Science Foundation of China (42372344).

#### References

- Abdar, M., Pourpanah, F., Hussain, S., Rezazadegan, D., Liu, L., Ghavamzadeh, M., Fieguth, P., Cao,  
615 X., Khosravi, A., and Acharya, U. R.: A review of uncertainty quantification in deep learning:  
Techniques, applications and challenges, *Information Fusion*, 76, 243–297,  
<https://doi.org/10.1016/j.inffus.2021.05.008>, 2021.
- Agterberg, F. P., Bonham-Carter, G. F., Cheng, Q., and Wright, D. F.: Weights of evidence modeling  
and weighted logistic regression for mineral potential mapping, *Computers in Geology*, 25, 13–32,  
620 1993.



- Aitchison, J.: The statistical analysis of compositional data, *Journal of the Royal Statistical Society: Series B (Methodological)*, 44(2), 139–160, <https://doi.org/10.1111/j.2517-6161.1982.tb01195.x>, 1982.
- Bárdossy, G.: Evaluation of Uncertainties and Risks in Geology, *New Mathematical Approaches for their Handling*, Springer, <https://doi.org/10.1007/978-3-662-07138-0>, 2004.
- Bárdossy, G., and Fodor, J.: Traditional and new ways to handle uncertainty in geology, *Natural Resources Research*, 10(3), 179–187, 2001.
- Blei, D. M., Kucukelbir, A., and McAuliffe, J. D.: Variational inference: A review for statisticians, Taylor & Francis, 859–877, <https://doi.org/10.1080/01621459.2017.1285773>, 2017.
- 630 Bonham-Carter, G.: *Geographic information systems for geoscientists: modelling with GIS*, Elsevier, <https://doi.org/10.1080/01431169608948997>, 1994.
- Burkin, J. N., Lindsay, M. D., Occhipinti, S. A., and Holden, E.: Incorporating conceptual and interpretation uncertainty to mineral prospectivity modelling, *Geoscience Frontiers*, 10(4), 1383–1396, <https://doi.org/10.1016/j.gsf.2019.01.009>, 2019.
- 635 Carranza, E., Hale, M., and Faassen, C.: Selection of coherent deposit-type locations and their application in data-driven mineral prospectivity mapping, *Ore Geology Reviews*, 33(3–4), 536–558, <https://doi.org/10.1016/j.oregeorev.2007.07.001>, 2008.
- Carranza, E. J. M.: Geochemical anomaly and mineral prospectivity mapping in GIS, 11, Elsevier, [https://doi.org/10.1016/S0168-6275\(08\)X0001-7](https://doi.org/10.1016/S0168-6275(08)X0001-7), 2008.
- 640 Chen, Y., and Wu, W.: A prospecting cost-benefit strategy for mineral potential mapping based on ROC curve analysis, *Ore Geology Reviews*, 74, 26–38, <https://doi.org/10.1016/j.oregeorev.2015.11.005>, 2016.
- Cheng, Q.: Mapping singularities with stream sediment geochemical data for prediction of undiscovered mineral deposits in Gejiu, Yunnan Province, China, *Ore Geology Reviews*, 32(1–2), 645 314–324, <https://doi.org/10.1016/j.oregeorev.2006.10.002>, 2007.
- Cheng, Q., and Agterberg, F. P.: Fuzzy weights of evidence method and its application in mineral potential mapping, *Natural Resources Research*, 8(1), 27–35, 1999.
- Deng, J., and Wang, Q.: Gold mineralization in China: Metallogenic provinces, deposit types and tectonic framework, *Gondwana Research*, 36, 219–274, <https://doi.org/10.1016/j.gr.2015.10.003>, 650 2016.



- Fakour, F., Mosleh, A., and Ramezani, R.: A structured review of literature on uncertainty in machine learning & deep learning, arXiv preprint arXiv:2406.00332, <https://doi.org/10.48550/arXiv.2406.00332>, 2024.
- Fan, H., Zhai, M., Yang, K., and Hu, F.: Late Mesozoic gold mineralization in the North China craton, 655 in: Main tectonic events and metallogeny of the North China craton, Springer, 511–525, [https://doi.org/10.1007/978-981-10-1064-4\\_21](https://doi.org/10.1007/978-981-10-1064-4_21), 2016.
- Fan, M., Xiao, K., Sun, L., and Xu, Y.: Metallogenic prediction based on geological-model driven and data-driven multisource information fusion: A case study of gold deposits in Xiong'er shan area, Henan Province, China, Ore Geology Reviews, 156, 105390, 660 <https://doi.org/10.1016/j.oregeorev.2023.105390>, 2023.
- Gal, Y.: Uncertainty in deep learning, University of Cambridge, 2016.
- Gal, Y., and Ghahramani, Z.: Dropout as a bayesian approximation: Representing model uncertainty in deep learning, International Conference on Machine Learning, 1050–1059, <https://doi.org/10.48550/arXiv.1506.02158>, 2016.
- 665 Gal, Y., and Ghahramani, Z.: Bayesian convolutional neural networks with Bernoulli approximate variational inference, arXiv preprint arXiv:1506.02158, <https://doi.org/10.48550/arXiv.1506.02158>, 2015.
- Gawlikowski, J., Tassi, C. R. N., Ali, M., Lee, J., Humt, M., Feng, J., Kruspe, A., Triebel, R., Jung, P., and Roscher, R.: A survey of uncertainty in deep neural networks, Artificial Intelligence Review, 670 56(Suppl 1), 1513–1589, <https://doi.org/10.1007/s10462-022-10244-5>, 2023.
- Gilks, W. R., Richardson, S., and Spiegelhalter, D.: Markov chain Monte Carlo in practice, CRC press, 1995.
- Gu, J., Wang, Z., Kuen, J., Ma, L., Shahroudy, A., Shuai, B., Liu, T., Wang, X., Wang, G., Cai, J., and Chen, T.: Recent advances in convolutional neural networks, Pattern recognition, 77, 354–377, 675 <https://doi.org/10.1016/j.patcog.2017.10.013>, 2018.
- Hosseini, S. T., Asghari, O., and Emery, X.: An enhanced direct sampling (DS) approach to model the geological domain with locally varying proportions: Application to Golgohar iron ore mine, Iran, Ore Geology Reviews, 139, 104452, <https://doi.org/10.1016/j.oregeorev.2021.104452>, 2021.



- Hüllermeier, E., and Waegeman, W.: Aleatoric and epistemic uncertainty in machine learning: An  
680 introduction to concepts and methods, *Machine Learning*, 110(3), 457–506,  
<https://doi.org/10.1007/s10994-021-05954-7>, 2021.
- Lisitsin, V. A., Porwal, A., and McCuaig, T. C.: Probabilistic fuzzy logic modeling: quantifying  
uncertainty of mineral prospectivity models using Monte Carlo simulations, *Mathematical  
Geosciences*, 46(6), 747–769, <https://doi.org/10.1007/s11004-014-9504-5>, 2014.
- 685 Liu, Y., Cheng, Q., Carranza, E. J. M., and Zhou, K.: Assessment of geochemical anomaly uncertainty  
through geostatistical simulation and singularity analysis, *Natural Resources Research*, 28(1),  
199–212, <https://doi.org/10.1007/s11053-018-9466-1>, 2019.
- Li, T., Zuo, R., Zhao, X., and Zhao, K.: Mapping prospectivity for regolith-hosted REE deposits via  
convolutional neural network with generative adversarial network augmented data, *Ore Geology  
690 Reviews*, 142, 104693, <https://doi.org/10.1016/j.oregeorev.2022.104693>, 2022.
- Lindi, O. T., Aladejare, A. E., Ozoji, T. M., and Ranta, J. P.: Uncertainty quantification in mineral  
resource estimation, *Natural Resources Research*, 33(6), 2503–2526,  
<https://doi.org/10.1007/s11053-024-09968-8>, 2024.
- Mao, J.: Mesozoic large-scale metallogenic pulses in North China and corresponding geodynamic  
695 settings, *Acta Petrologica Sinica*, 21, 169–188, [https://doi.org/10.1016/S1875-5364\(05\)80015-7](https://doi.org/10.1016/S1875-5364(05)80015-7),  
2005.
- Mao, J., Goldfarb, R. J., Zhang, Z., Xu, W., Qiu, Y., and Deng, J.: Gold deposits in the Xiaqingling–  
Xiong'ershan region, Qinling Mountains, central China, *Mineralium Deposita*, 37(3), 306–325,  
<https://doi.org/10.1007/s00126-002-0165-7>, 2002.
- 700 Mao, J., Qiu, Y., Goldfarb, R. J., Zhang, Z., Garwin, S., and Fengshou, R.: Geology, distribution, and  
classification of gold deposits in the western Qinling belt, central China, *Mineralium Deposita*,  
37(3), 352–377, <https://doi.org/10.1007/s00126-002-0170-x>, 2002.
- Mariethoz, G., Renard, P., and Straubhaar, J.: The direct sampling method to perform multiple-point  
geostatistical simulations, *Water Resources Research*, 46(11),  
705 <https://doi.org/10.1029/2009WR008650>, 2010.
- Meerschman, E., Piro, G., Mariethoz, G., Straubhaar, J., Van Meirvenne, M., and Renard, P.: A  
practical guide to performing multiple-point statistical simulations with the Direct Sampling



- algorithm, *Computers & Geosciences*, 52, 307–324, <https://doi.org/10.1016/j.cageo.2012.10.009>, 2013.
- 710 Mena, J., Pujol, O., and Vitrià, J.: A survey on uncertainty estimation in deep learning classification systems from a bayesian perspective, *ACM Computing Surveys (CSUR)*, 54(9), 1–35, <https://doi.org/10.1145/3450626>, 2021.
- Pang, Z., Gao, F., Du, Y., Du, Y., Zong, Z., Xie, J., and Xin, F.: Late Jurassic to Early Cretaceous magmatism in the Xiong’ershan gold district, central China: implications for gold mineralization and geodynamics, *Geological Magazine*, 157(3), 435–457, <https://doi.org/10.1017/S001675681900022X>, 2020.
- 715 Seoh, R.: Qualitative analysis of monte carlo dropout, arXiv preprint arXiv:2007.01720, <https://doi.org/10.48550/arXiv.2007.01720>, 2020.
- Shannon, C. E.: A mathematical theory of communication, *The Bell System Technical Journal*, 27(3), 720 379–423, <https://doi.org/10.1002/j.1538-7305.1948.tb01338.x>, 1948.
- Shi, Z., Zuo, R., and Zhou, B.: Deep reinforcement learning for mineral prospectivity mapping, *Mathematical Geosciences*, 55(6), 773–797, <https://doi.org/10.1007/s11004-023-09967-4>, 2023.
- Shridhar, K.: Bayesian convolutional neural network, University of Kaiserslautern, 2019.
- Shridhar, K., Laumann, F., and Liwicki, M.: A comprehensive guide to bayesian convolutional neural network with variational inference, arXiv preprint arXiv:1901.02731, 725 <https://doi.org/10.48550/arXiv.1901.02731>, 2019.
- Tang, K., Li, J., Selby, D., Zhou, M., Bi, S., and Deng, X.: Geology, mineralization, and geochronology of the Qianhe gold deposit, Xiong’ershan area, southern North China Craton, *Mineralium Deposita*, 48(6), 729–747, <https://doi.org/10.1007/s00126-013-0526-7>, 2013.
- 730 Wang, H., and Yeung, D.: A survey on Bayesian deep learning, *ACM Computing Surveys (csur)*, 53(5), 1–37, <https://doi.org/10.1145/3357223>, 2020.
- Wang, J., and Zuo, R.: Recognizing geochemical anomalies via stochastic simulation-based local singularity analysis, *Journal of Geochemical Exploration*, 198, 29–40, <https://doi.org/10.1016/j.gexplo.2018.12.004>, 2019.
- 735 Wang, Z., Zuo, R., and Zhang, Z.: Spatial analysis of Fe deposits in Fujian Province, China: Implications for mineral exploration, *Journal of Earth Science*, 26(6), 813–820, <https://doi.org/10.1007/s12583-015-0534-4>, 2015.



- Wang, Z., Yin, Z., Caers, J., and Zuo, R.: A Monte Carlo-based framework for risk-return analysis in mineral prospectivity mapping, *Geoscience Frontiers*, 11(6), 2297–2308, 740 <https://doi.org/10.1016/j.gsf.2020.05.009>, 2020.
- Wang, Z., and Zuo, R.: Mineral prospectivity mapping using a joint singularity-based weighting method and long short-term memory network, *Computers & Geosciences*, 158, 104974, <https://doi.org/10.1016/j.cageo.2022.104974>, 2022.
- Wang, Z., Zuo, R., and Yang, F.: Geological mapping using direct sampling and a convolutional neural 745 network based on geochemical survey data, *Mathematical Geosciences*, 55(7), 1035–1058, <https://doi.org/10.1007/s11004-023-09990-7>, 2023.
- Wang, Z., Zuo, R., and Kreuzer, O. P.: Uncertainty Quantification of Deep Learning Algorithms for Lithological Mapping, *Mathematical Geosciences*, 58, 503–531, <https://doi.org/10.1007/s11004-025-10235-z>, 2026.
- 750 Wellmann, J. F., and Regenauer-Lieb, K.: Uncertainties have a meaning: Information entropy as a quality measure for 3-D geological models, *Tectonophysics*, 526, 207–216, <https://doi.org/10.1016/j.tecto.2011.11.004>, 2012.
- Wu, F., Gong, Q., Shi, J., Li, J., and Wang, Z.: Ore-controlling geological factors of gold deposits in the Xiong’ershan region, western Henan Province, *Geology & Exploration*, 48, 865–875, 2012.
- 755 Xiong, Y., and Zuo, R.: Recognition of geochemical anomalies using a deep autoencoder network, *Computers & Geosciences*, 86, 75–82, <https://doi.org/10.1016/j.cageo.2016.05.002>, 2016.
- Xiong, Y., Zuo, R., and Carranza, E. J. M.: Mapping mineral prospectivity through big data analytics and a deep learning algorithm, *Ore Geology Reviews*, 102, 811–817, <https://doi.org/10.1016/j.oregeorev.2018.10.006>, 2018.
- 760 Xie, X., Mu, X., and Ren, T.: Geochemical mapping in China, *Journal of Geochemical Exploration*, 60(1), 99–113, 1997.
- Yang, F., Wang, Z., Zuo, R., Sun, S., and Zhou, B.: Quantification of uncertainty associated with evidence layers in mineral prospectivity mapping using direct sampling and convolutional neural 765 network, *Natural Resources Research*, 32(1), 79–98, <https://doi.org/10.1007/s11053-022-09901-6>, 2023.



- Yang, F., and Zuo, R.: Geologically constrained convolutional neural network for mineral prospectivity mapping, *Mathematical Geosciences*, 56(8), 1605–1628, <https://doi.org/10.1007/s11004-024-09947-z>, 2024.
- 770 Yang, F., Zuo, R., and Kreuzer, O. P.: Artificial intelligence for mineral exploration: A review and perspectives on future directions from data science, *Earth-Science Reviews*, 258, 104941, <https://doi.org/10.1016/j.earscirev.2024.104941>, 2024.
- Yang, F., Zuo, R., Xiong, Y., Xu, Y., Nie, J., and Zhang, G.: Dual-branch convolutional neural network and its post hoc interpretability for mapping mineral prospectivity, *Mathematical Geosciences*, 56(7), 1487–1515, <https://doi.org/10.1007/s11004-024-09938-y>, 2024.
- 775 Yin, B., Zuo, R., and Xiong, Y.: Mineral prospectivity mapping via gated recurrent unit model, *Natural Resources Research*, 31(4), 2065–2079, <https://doi.org/10.1007/s11053-021-09826-7>, 2022.
- Zhang, L., Bai, Y., Zhu, M., Huang, K., and Peng, Z.: Regional heterogeneous temporal–spatial distribution of gold deposits in the North China Craton: A review, *Geological Journal*, 55(8), 5646–5663, <https://doi.org/10.1002/gj.3765>, 2020.
- 780 Zuo, R.: Geodata science-based mineral prospectivity mapping: A review, *Natural Resources Research*, 29(6), 3415–3424, <https://doi.org/10.1007/s11053-020-09700-9>, 2020.
- Zuo, R.: A nonlinear controlling function of geological features on magmatic–hydrothermal mineralization, *Scientific Reports*, 6(1), 27127, <https://doi.org/10.1038/srep27127>, 2016.
- Zuo, R.: Key technology for intelligent mineral prospectivity mapping: Challenges and solutions, *Science China Earth Sciences*, 68(9), 2976–2991, <https://doi.org/10.1007/s11430-024-1406-9>, 2025.
- 785 Zuo, R., Cheng, Q., Xu, Y., Yang, F., Xiong, Y., Wang, Z., and Kreuzer, O. P.: Explainable artificial intelligence models for mineral prospectivity mapping, *Science China Earth Sciences*, 67(9), 2864–2875, <https://doi.org/10.1007/s11430-024-1391-7>, 2024.
- 790 Zuo, R., Kreuzer, O. P., Wang, J., Xiong, Y., Zhang, Z., and Wang, Z.: Uncertainties in GIS-based mineral prospectivity mapping: Key types, potential impacts and possible solutions, *Natural Resources Research*, 30(5), 3059–3079, <https://doi.org/10.1007/s11053-021-09801-4>, 2021.
- Zuo, R., and Wang, Z.: Effects of random negative training samples on mineral prospectivity mapping, *Natural Resources Research*, 29(6), 3443–3455, <https://doi.org/10.1007/s11053-020-09706-3>, 2020.
- 795



- Zuo, R., Xiong, Y., Wang, J., and Carranza, E. J. M.: Deep learning and its application in geochemical mapping, *Earth-Science Reviews*, 192, 1–14, <https://doi.org/10.1016/j.earscirev.2018.12.009>, 2019.
- Zuo, R., Xiong, Y., Wang, Z., Wang, J., and Kreuzer, O. P.: A new generation of artificial intelligence algorithms for mineral prospectivity mapping, *Natural Resources Research*, 32(5), 1859–1869, <https://doi.org/10.1007/s11053-023-09936-4>, 2023.
- Zuo, R., and Xu, Y.: Graph deep learning model for mapping mineral prospectivity, *Mathematical Geosciences*, 55(1), 1–21, <https://doi.org/10.1007/s11004-022-09920-9>, 2023.
- Zuo, R., Yang, F., Cheng, Q., and Kreuzer, O. P.: A novel data-knowledge dual-driven model coupling artificial intelligence with a mineral systems approach for mineral prospectivity mapping, *Geology*, 53(3), 284–288, <https://doi.org/10.1130/G52194.1>, 2025.
- Zuo, R., Zhang, Z., Zhang, D., Carranza, E. J. M., and Wang, H.: Evaluation of uncertainty in mineral prospectivity mapping due to missing evidence: a case study with skarn-type Fe deposits in Southwestern Fujian Province, China, *Ore Geology Reviews*, 71, 502–515, <https://doi.org/10.1016/j.oregeorev.2015.01.002>, 2015.